Fictitious phase separation in Li layered oxides driven by electro-autocatalysis

Jungjin Park ^{1,2,3,9}, Hongbo Zhao ^{4,9}, Stephen Dongmin Kang ^{1,9}, Kipil Lim^{1,2,5,6}, Chia-Chin Chen¹, Young-Sang Yu ³, Richard D. Braatz ⁴, David A. Shapiro ³, Jihyun Hong ^{1,2,5,6,7}, Michael F. Toney^{5,6}, Martin Z. Bazant ^{4,8} and William C. Chueh ^{1,2,6}

Layered oxides widely used as lithium-ion battery electrodes are designed to be cycled under conditions that avoid phase transitions. Although the desired single-phase composition ranges are well established near equilibrium, operando diffraction studies on many-particle porous electrodes have suggested phase separation during delithiation. Notably, the separation is not always observed, and never during lithiation. These anomalies have been attributed to irreversible processes during the first delithiation or reversible concentration-dependent diffusion. However, these explanations are not consistent with all experimental observations such as rate and path dependencies and particle-by-particle lithium concentration changes. Here, we show that the apparent phase separation is a dynamical artefact occurring in a many-particle system driven by autocatalytic electrochemical reactions, that is, an interfacial exchange current that increases with the extent of delithiation. We experimentally validate this population-dynamics model using the single-phase material $\text{Li}_x(\text{Ni}_{1/3}\text{Mn}_{1/3}\text{Co}_{1/3})\text{O}_2$ (0.5 < x < 1) and demonstrate generality with other transition-metal compositions. Operando diffraction and nanoscale oxidation-state mapping unambiguously prove that this fictitious phase separation is a repeatable non-equilibrium effect. We quantitatively confirm the theory with multiple-datastream-driven model extraction. More generally, our study experimentally demonstrates the control of ensemble stability by electro-autocatalysis, highlighting the importance of population dynamics in battery electrodes (even non-phase-separating ones).

nderstanding phase diagrams, whether it be for equilibrium (for example, temperature-composition) or kinetics (for example, time-temperature-transformation), is fundamental in materials science. Careful attention to rate and path dependence is crucial for distinguishing equilibrium and kinetic effects in phase behaviour, and battery materials are no exception to this basic prescription. The dynamics associated with the many-particle (ensemble) structure in battery electrodes^{1,2} (for example, inter- and intra-particle phase separation) only make such rate and path dependencies ever more critical. In phase-separating LiFePO₄, for example, it has been recognized that the reaction rate determines both the emergence of a thermodynamically forbidden solid solution³⁻⁵ as well as the transition from particle-by-particle behaviour to concurrent intercalation^{1,6}. Recently, rate-dependent pathways have also been suggested in Li₄Ti₅O₁₂ (refs. ^{7,8}). All these non-equilibrium phenomena contribute to the excellent rate capability of these materials.

Meanwhile, in the so-called solid-solution layered oxides, studies on phase evolution have not been as comprehensive since this material class is deemed a single phase. Included are compounds such as Li(Ni,Mn,Co)O₂ (NMC) and Li(Ni,Co,Al)O₂ (NCA), typically viewed as having extensive single-phase composition ranges down to a lithium fraction of at least 0.5. This standard view is based on monotonic Nernst potential profiles and X-ray diffraction (XRD) data on equilibrated samples⁹⁻¹⁴.

Contradicting the standard view, phase separation at more than half lithium filling has also been reported in numerous operando XRD studies $^{15-22}$. This anomaly has been observed during the first charge, but not during the following discharge. At the rates used in these studies, the effect did not repeat on the second cycle, leading to the prevailing view that the anomaly is a 'first-cycle effect' $^{17-19}$. Surface passivation by $\rm Li_2CO_3$ has been suggested as one cause 19 . More recently, apparent phase separation has also been reported in the second cycle, attributed to sluggish lithium diffusion near fully lithiated compositions 22 . Other authors maintain that the observed phases are equilibrium phases 15,16,21 , designating them as H1 and H2 phases analogous to LiNiO $_2$ (ref. 23).

However, rate and path dependencies have not been comprehensively addressed for any NMC or NCA composition, despite their widespread use²⁴. Partly responsible are the restricted designs of operando experiments based on available instrument time, limiting the range of rates and cycles. Likewise, the lack of particle-resolved composition mapping across an ensemble makes it difficult to assess nanoscale variations that arise from reaction and transport limitations. For these reasons, and despite the success of porous electrode theory^{25–27}, a quantitative and predictive model explaining the rate and path dependencies in layered oxides has not been developed.

Here, we report that the apparent phase separation persists in later cycles, even in LiNi_{1/3}Mn_{1/3}Co_{1/3}O₂ (NMC111) and

¹Department of Materials Science and Engineering, Stanford University, Stanford, CA, USA. ²Stanford Institute for Materials & Energy Sciences, SLAC National Accelerator Laboratory, Menlo Park, CA, USA. ³Advanced Light Source, Lawrence Berkeley National Laboratory, Berkeley, CA, USA. ⁴Department of Chemical Engineering, Massachusetts Institute of Technology, Cambridge, MA, USA. ⁵Stanford Synchrotron Radiation Lightsource, SLAC National Accelerator Laboratory, Menlo Park, CA, USA. ⁶Applied Energy Division, SLAC National Accelerator Laboratory, Menlo Park, CA, USA. ⁷Center for Energy Materials Research, Korea Institute of Science and Technology, Seoul, Korea. ⁸Department of Mathematics, Massachusetts Institute of Technology, Cambridge, MA, USA. ⁹These authors contributed equally: Jungjin Park, Hongbo Zhao, Stephen Dongmin Kang. [™]e-mail: jihyunh@kist.re.kr; bazant@mit.edu; wchueh@stanford.edu

LiNi_{0.5}Mn_{0.3}Co_{0.2}O₂ (NMC532), considered the most stable among the NMC and NCA families. We also find similar behaviour in Ni-rich and Li/Mn-rich compositions. Rate-varied operando XRD shows that the separation is triggered above a threshold rate, and only for delithiation, not lithiation. We perform nanoscale X-ray microscopy on more than 100 primary particles and show that a non-unimodal composition distribution exists not within the particles but between the particles. We rule out diffusion-based mechanisms, concluding that reaction-limited (solo-) autocatalytic behaviour (that is a particle-wise reaction rate accelerating upon progression) causes the non-unimodal distribution in particle-to-particle composition. We formulate a model that explains the rate and path dependencies of phase evolution, reconciling the seemingly contradictory literature reports. Our findings highlight the importance of population dynamics, even for non-separating single-phase materials. Crucially, we challenge the conventional wisdom that diffusion determines the inter-particle compositional inhomogeneity and establish that controlling the reaction kinetics holds the key towards controlling ensemble systems.

Fast-rate-induced fictitious phase separation. To assess the role of secondary particle structure and first-cycle effects, we prepared composite electrodes consisting of both agglomerate particles (size = $10-15 \,\mu\text{m}$, Fig. 1a) and platelet particles (size = $1-2 \,\mu\text{m}$, Fig. 1d) of NMC111. To minimize transport effects from the electrolyte and current collector, we used a low active material loading (NMC111:carbon black:binder = 4:4:2 by weight) and a thin electrode (~20 µm), and confirmed that transport is not limiting (Supplementary Fig. 3). One slow-forming cycle at C/20 was carried out while re-lithiating to an average lithium fraction of >0.95 during the first discharge, where 1C is defined based on the lithium fraction changing by 1.0. We carried out operando XRD measurements on pouch cells uniformly pressurized between beryllium plates (Supplementary Fig. 25) during the second and tenth cycles (charge and discharge) and monitored the evolution of the (003) Bragg peak at several cycling rates.

The rate and direction of the current-driven reaction were found to be the primary factors inducing the apparent phase separation, rather than first-cycle forming or particle morphology, as shown in Fig. 1. Bifurcation of the (003) peak is seen during fast delithiation (Fig. 1b,e). By contrast, during fast lithiation, a single (003) peak shifts continuously with lithium content, consistent with a single-phase reaction. This continuous shift is also seen for slow cycling (Fig. 1c,f). Even at subsequent cycles, the dichotomy between fast and slow regimes persists. The tenth-cycle operando XRD data (Supplementary Figs. 5 and 6) show behaviour similar to that of the second cycle. We also observe the phenomenon with NMC532 (Extended Data Fig. 1), with a Ni-rich chemistry (LiNi_{0.83} $Mn_{0.05}Co_{0.12}O_2$, NMC 83:5:12; Extended Data Fig. 2) and with a Li/ Mn-rich chemistry (Li_{1.17}Ni_{0.21}Mn_{0.54}Co_{0.08}O₂, LMR-NMC; Extended Data Fig. 3). It should be noted that the different particle morphologies and transition-metal compositions make the specific delithiation rates not directly comparable. Therefore, we define 'fast' and 'slow' by the qualitative distinction of delithiation behaviour, rather than by a specific C-rate.

The important feature from the operando XRD measurement is that an electrode can be driven into distinct pathways, fast and slow, during any cycle. The two apparent phases, referred to as H1 and H2 in the literature, are in fact identical in crystal structures¹⁵. Since H1 can be transformed into H2 without a phase transition (slow cycles in Fig. 1), H1 and H2 must be thermodynamically identical phases. In other words, the phase separation must be a fictitious one where no actual phase transition occurs.

Inter-particle inhomogeneity responsible for the fictitious phases. To understand the microscopic details underlying the fictitious phase

separation, we probed the composition distribution among the particles. With only XRD, it is challenging to distinguish whether overall inhomogeneity is dominated by the lithium concentration profiles inside the particles (intra-particle) or by variations between the particles (inter-particle). To access this information, we cycled platelet particles (Fig. 1d) to average lithium fractions of 0.75 and 0.50, on the second charge and discharge. Then, we 'quenched' the lithium exchange between the particles by removing the electrodes from the electrolyte within two minutes after current interruption, immediately followed by rinsing with diethyl carbonate. The particles were dispersed and imaged using X-ray spectromicroscopy (Ni L-edge, from which the lithium composition is determined; Supplementary Fig. 8) with a 50 nm step size. This preparation was done at least one day ahead of imaging to allow the intra-particle distribution to approach equilibrium (particle sizes 1-2 μm) while leaving the inter-particle distribution quenched. Thus, it can be determined whether the fictitious separation occurs within or between the particles.

Nanoscale lithium composition maps measured on more than 100 particles, summarized in Fig. 2, reveal that the fictitious phase separation arises from inter-particle rather than intra-particle compositional variation. During fast delithiation, we observed an unusual non-unimodal composition distribution (Fig. 2a), where a large number of particles are still in their nearly lithiated (unreacted) state (red) as well as their delithiated (reacted) state (green). From the microscopy results, we reconstructed a bifurcated XRD peak from the areal statistics in Fig. 2a, as shown in Supplementary Fig. 10. This consistency shows that the quenching procedure was successful and further indicates that inter-particle inhomogeneity is the dominant origin for the fictitious phase separation seen during operando XRD (we further confirm this result by measuring the diffraction on a quenched electrode; Supplementary Fig. 27). This result will later be shown to have important implications on the role of reaction and diffusion limitations. Under all other conditions (Fig. 2b-h), including fast lithiation, we observed the typical unimodal composition distribution, consistent with the XRD measurements.

The equilibrium intra-particle lithium composition is largely homogeneous, even in the fast-delithiated state with particles of various average lithium fractions (Fig. 2a; see Supplementary Fig. 9 for line profiles). This homogeneity further supports that the equilibrium state is a single phase.

Heterogeneity evolution in autocatalytic and autoinhibitory reactions. Having confirmed that the XRD peak bifurcation during fast delithiation arises from the unequal progression of different particles (rather than phase separation), it remains unclear why NMC111 develops a non-unimodal composition distribution. If one particle happens to react before another, that reacted particle has a diminished driving force for further reaction, which would normally suppress inhomogeneity (negative feedback). Therefore, to explain the fictitious phase separation, there must be a countering mechanism (positive feedback).

Identifying the source of positive feedback is key to understanding this type of self-reinforcing or autocatalytic behaviour. For example, in thermal runaways, a common concern for lithium-ion batteries²⁸, the large heat generated from device failure further accelerates the failure.

By postulating a kinetic rate that increases steeply with delithiation, we explain not only the fast-rate-induced fictitious phase separation during delithiation, but also the absence of such separation during lithiation. Recall that the equilibrium state in NMC111 consists of particles of uniform composition. During fast delithiation, we observe fictitious phase separation, which implies that the particle ensemble is far from equilibrium and is dominated by kinetics. Specifically, what we have defined as 'fast' could be understood as when the current-driven reaction rate is much faster than the equilibration rate (Fig. 3a). Then, when inter-particle inhomogeneity

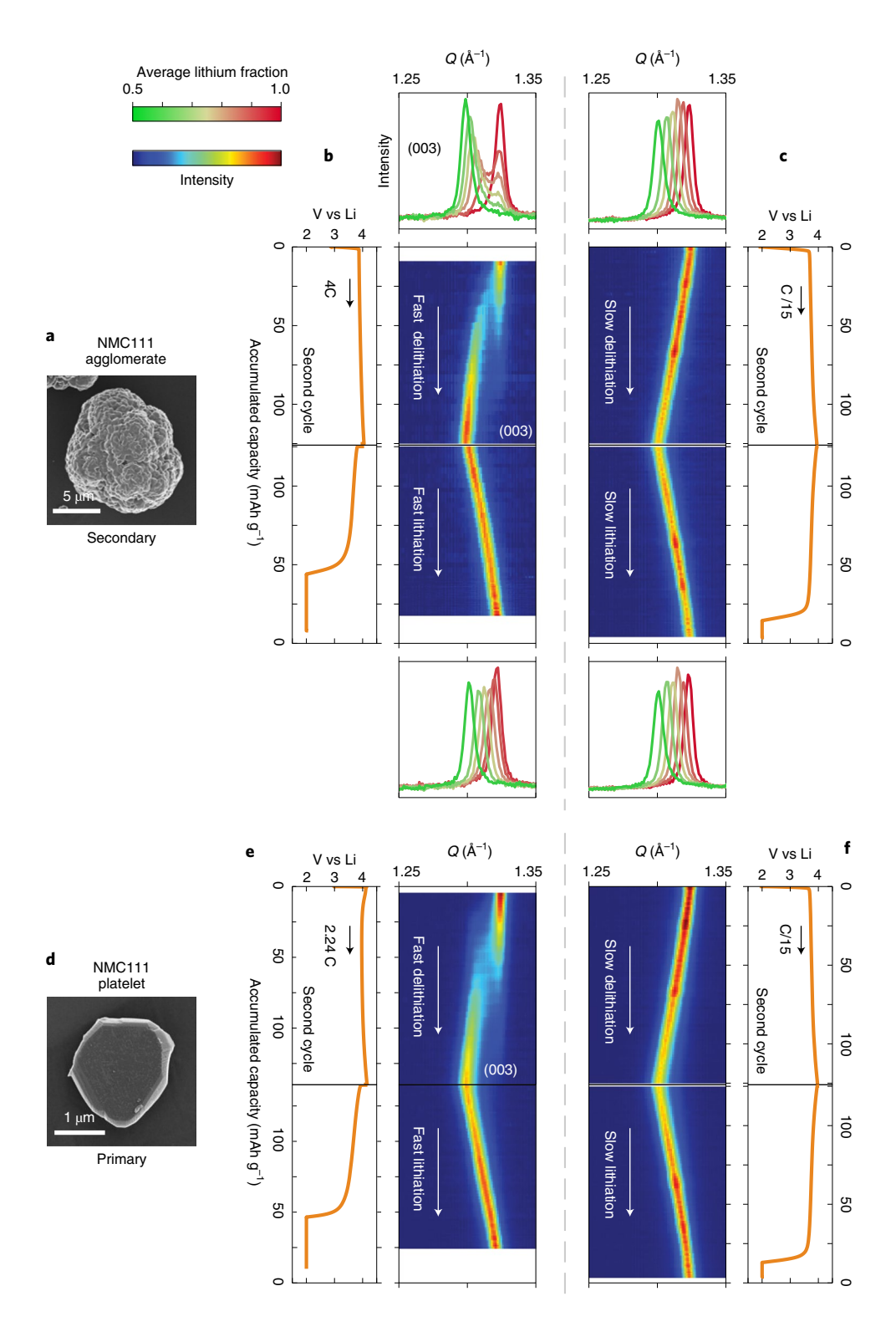


Fig. 1 | Phase evolution of $\text{Li}_x(\text{Ni}_{l/3}\text{Mn}_{l/3}\text{Co}_{l/3})\text{O}_2$ during the second cycle at different cycling currents, probed with operando XRD. a-c, SEM image of agglomerate particles (a) used for experiments with fast (4C) (b) and slow (C/15) (c) cycling currents. Diffraction and electrochemistry data are combined to share the capacity axes. The intensity image plots of the (003) peak show bifurcation during fast delithation, whereas continuous linear shifts are seen in other conditions. The line plots of the (003) peak at selected average lithium fractions show a non-unimodal evolution in the fast-delithiation condition, as opposed to the progressive shift in other conditions. **d-f**, SEM image of platelet particles (**d**) used for experiments with fast (2.24C) (e) and slow (C/15) (f) cycling currents. Overall behaviour is similar to that seen with agglomerate particles. The starting average lithium fractions, estimated from diffraction, are 1.00, 0.96, 1.00 and 0.99 with \pm 0.02 for **b**, **c**, **e** and **f**, respectively. Full lithiation at the end of the forming cycle was achieved through a voltage hold (2 V for this data set; similar experiments done with a 2.5 V hold showed similar results).

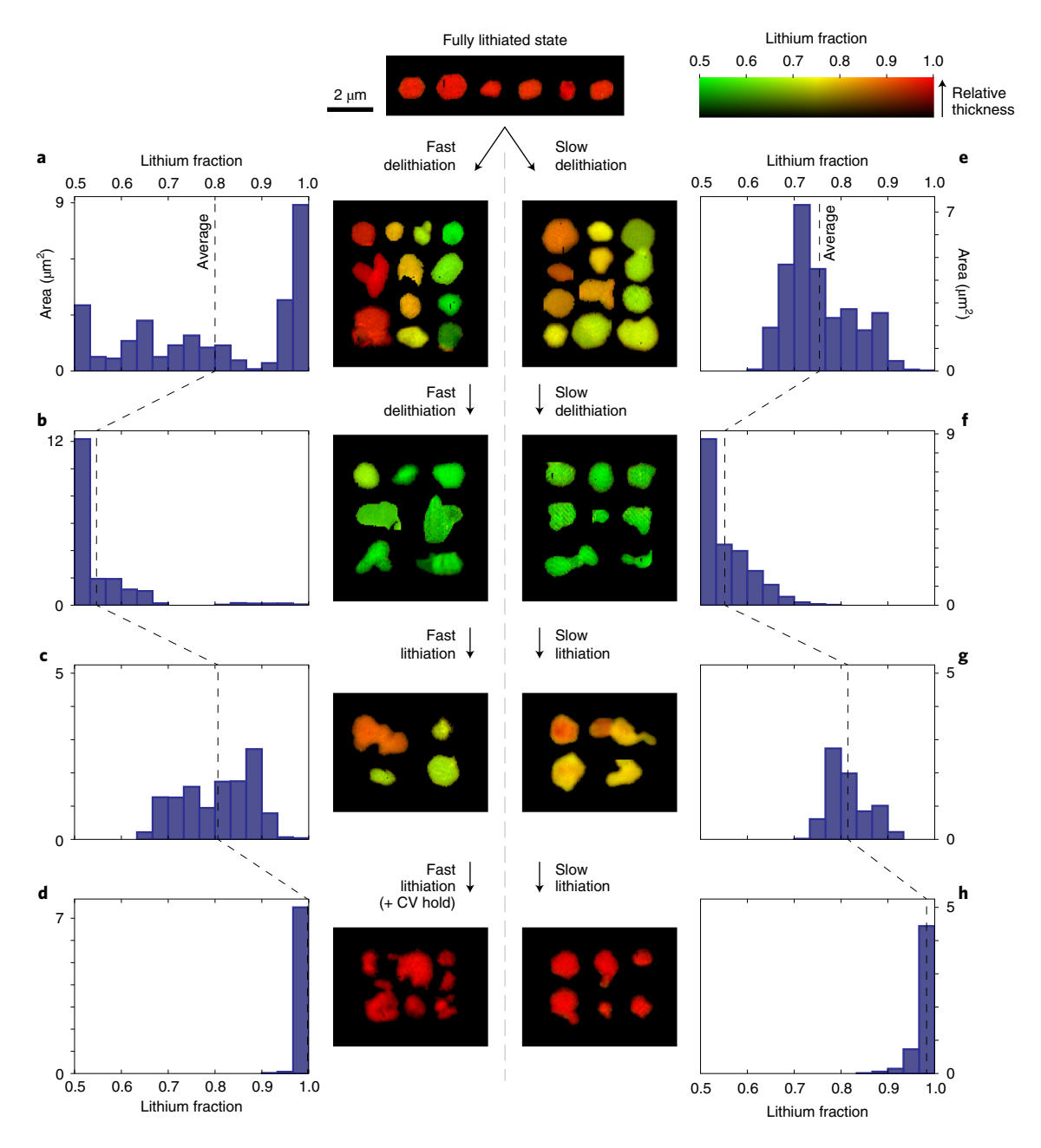


Fig. 2 | Lithium composition maps of individual platelet particles quenched at different overall states-of-charge during the second cycle, imaged with scanning transmission X-ray microscopy. \mathbf{a} - \mathbf{d} Particles sampled from fast-cycled (2C) cells during the second cycle at states-of-charge corresponding to average lithium fractions of $0.75 \rightarrow 0.50 \rightarrow 0.75 \rightarrow 1.00$ (accumulated capacity $70 \rightarrow 139 \rightarrow 70 \rightarrow 0$ mAh g⁻¹, respectively), which were controlled electrochemically. A constant voltage (CV) hold was applied at the end of the cycle to achieve full lithiation. \mathbf{e} - \mathbf{h} Particles sampled from slow-cycled (C/20) cells during the second cycle at states-of-charge identical to those of \mathbf{a} - \mathbf{d} , respectively. The average lithium fraction of each sample determined by the areal average of each particle is shown with dashed lines, approximately corresponding to the electrochemical state-of-charge. The fast-delithiation condition shows an inter-particle, non-unimodal composition distribution in \mathbf{a} before merging into a unimodal distribution at an overall lithium fraction of about 0.5 in \mathbf{b} . In all other conditions, a unimodal composition distribution is maintained. Only a selected number or particle images are shown for some conditions; see Supplementary Information for the images of all particles included in the histograms.

occurs for *any* reason, its evolution can follow two opposite pathways. In an autocatalytic case (Fig. 3c), the already-reacted particles are forced to react further (for example, constant current charging will force the overall reaction rate), resulting in a non-unimodal composition distribution of particles. Delithiation of NMC111 corresponds to this case. In the opposite case, that is, autoinhibitory or autoinhibitive (Fig. 3d), the unreacted particles will 'catch up' when the reaction is forced, suppressing the inhomogeneity. Since lithiation of NMC111 is the opposite reaction direction to the autocatalytic

direction, lithiation should be autoinhibitory. This argument is indeed consistent with the experiment (Fig. 3 is drawn on a general reaction coordinate, and the colour scheme is matched to that of the delithiation path as presented in Fig. 2).

Note that microstructure inhomogeneity cannot explain the contrast between delithiation and lithiation. Operando experiments on an intentionally heterogeneous electrode show peak bifurcation in both directions (Supplementary Fig. 26 and Supplementary Section 13). Also, previous explanations based on irreversible forming is

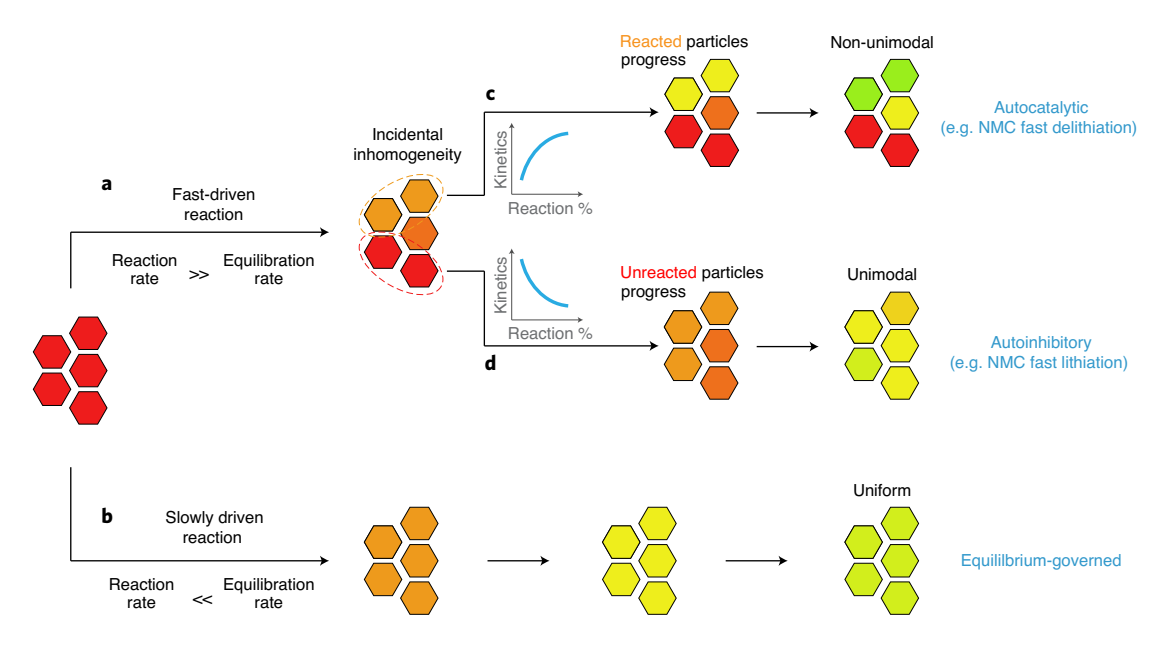


Fig. 3 | Autocatalytic and autoinhibitory reactions in electrochemically driven systems. **a**, Fast-driven pathway. Non-equilibrium behaviour originates from having a reaction rate that is much faster than the equilibration rate. **b**, Slowly driven pathway. The reaction progresses through equilibrium states. In the fast-driven case, incidental inhomogeneity in particle states can evolve largely following two qualitatively different pathways. **c**, When the reaction kinetics increase as the reaction progresses, reacted particles are favoured to progress further, resulting in a particle ensemble with a non-unimodal distribution (autocatalytic). **d**, If the reaction kinetics decrease as the reaction progresses, inhomogeneity is suppressed to yield a distribution that resembles the slowly driven reaction pathway (autoinhibitory).

not consistent with the repeated occurrence of direction-dependent peak bifurcation in later cycles.

Fictitious phase separation caused by reactions, not diffusion. Given the composition-dependent lithium diffusivity in layered oxides²², it is tempting to connect the autocatalytic behaviour illustrated in Fig. 3a to a diffusion-controlled process that becomes faster with delithiation. To assess this hypothesis, the general features of diffusion-induced composition profiles need to be understood in the context of composition distributions within and between the particles. We develop a particle ensemble model that simulates diffusion and reaction kinetics in the presence of statistical distributions such as particle size variations (see Supplementary Sections 5 and 6).

Apparently, fictitious phase separation can be produced in a diffusion-limited case by assuming a diffusion rate that increases exponentially upon delithiation (Fig. 4a). The simulated operando XRD image plot for an electrode consisting of 1,000 particles shows peak bifurcation during fast delithiation but not during lithiation, appearing to confirm the hypothesis. To compare with X-ray microscopy images, we also simulated the intra-particle equilibration while suppressing inter-particle Li exchange. Interestingly, the non-unimodal composition distribution, corresponding to the XRD peak bifurcation, reverts to a unimodal distribution. This relaxation occurs because diffusion induces compositional gradients inside the particle (that is, a diffusion front) but not between particles (Supplementary Fig. 14), regardless of the particle size distribution assumed. This simulated result contradicts the non-unimodal distribution in particle-to-particle composition, observed by microscopy (Fig. 2) and diffraction on quenched electrodes (Supplementary Fig. 27).

Next, we consider interface-limited delithiation kinetics, controlled by the surface reaction at the particle/electrolyte interface. By considering an exchange current that increases exponentially with the extent of delithiation, fictitious phase separation is similarly predicted (Fig. 4b). The important difference is that, in contrast to the diffusion-limited case, the interface-limited case successfully captures the experimentally observed inter-particle

non-unimodal composition distribution. Even after equilibration while suppressing inter-particle Li exchange, the non-unimodal composition distribution persists. The conclusion that interfacial reaction is limiting is also consistent with the electrochemistry, which shows current–voltage curves indicative of reaction limitation (Supplementary Fig. 3).

The qualitative difference between diffusion- and reactioninduced compositional inhomogeneity, summarized in Fig. 4c, is not well recognized in the literature. In fact, diffusion limitation has been suggested as a cause for inter-particle inhomogeniety in NCA²². In a bulk diffusion-controlled situation, diffusional fronts move from the particle/electrolyte interface to the interior of the particles. Because this diffusion process is slower than reaction rates at the interface in diffusion limitation, the particle/electrolyte interface will tend to the same composition in each particle. Therefore, diffusion cannot trigger preferential reactions between particles as they have similar compositions at the active surface. Particle-to-particle variations in the particle-averaged compositions will then simply reflect the non-uniformity of particle properties such as size. Diffusion may broaden the composition distribution, but it cannot generate an inter-particle non-unimodal distribution. Supplementary Video 1 illustrates the distinctive roles of diffusionand reaction-limited cases. Since diffusion limitation inherently counteracts inter-particle inhomogeneity, a mixed-control regime is also unlikely (see Supplementary Fig. 12). These results are consistent with the conclusions from a kinetics study on single particles²⁹.

These general conclusions about diffusion-induced inhomogeneity do not rely on the absolute values of particle size $R_{\rm p}$, chemical diffusivity D or C-rate used in the simulation: the controlling parameter for diffusion-limited dynamics is the ratio between $D/R_{\rm p}^2$ (the equilibration rate for diffusion) and the C-rate (the driven reaction rate)³⁰. Regardless of how these parameters are combined to produce fictitious phase separation, the qualitative behaviour is similar.

Interface limitation is the fundamental cause of inter-particle heterogeneity. The kinetic character underlying inter- and

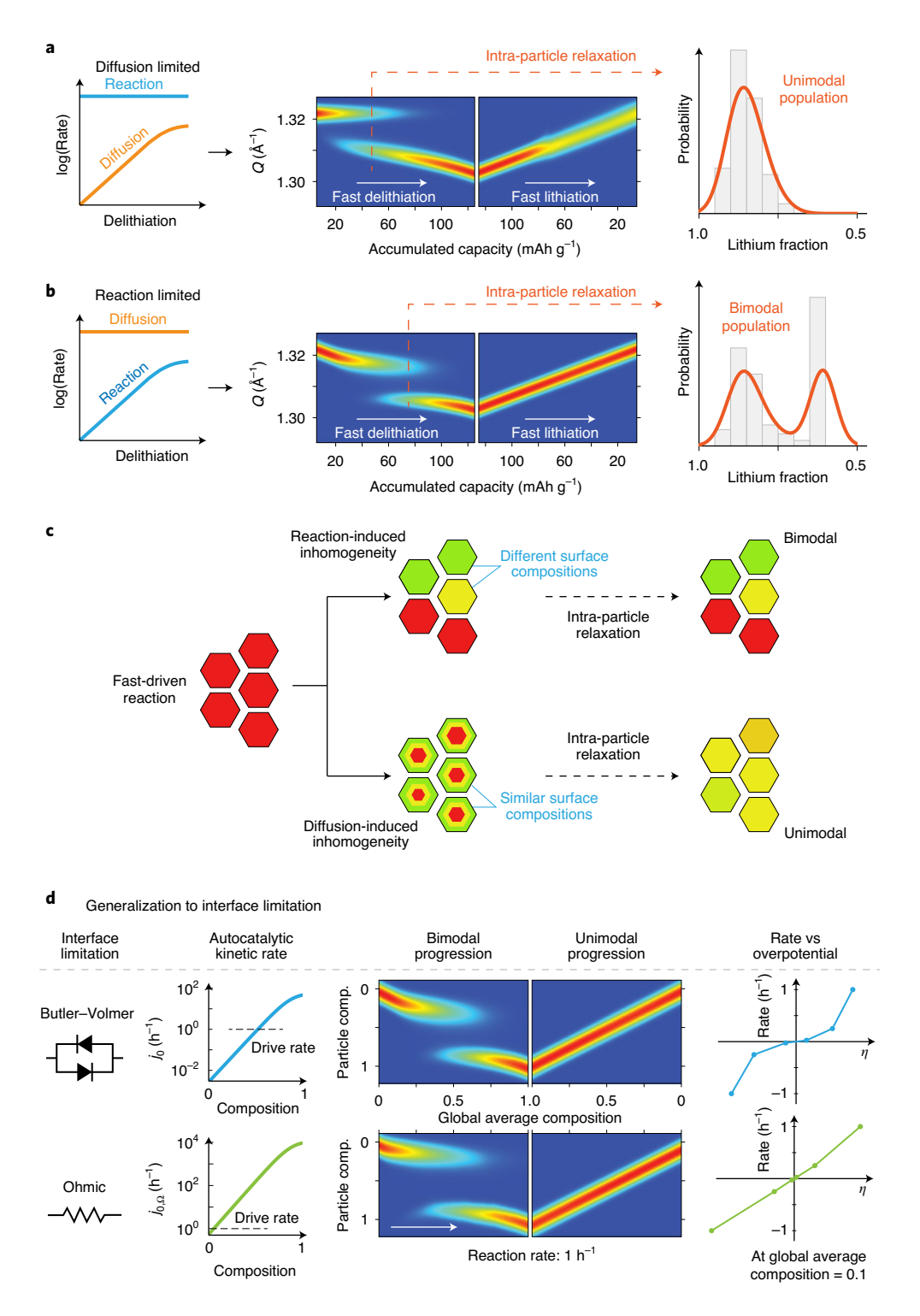


Fig. 4 | Inter-particle inhomogeneity from interface limitation and intra-particle inhomogeneity from solid-diffusion limitation. Using an ensemble of >1,000 particles, composition maps are simulated for fast-driven cycles in two different regimes (\mathbf{a} , \mathbf{b}). \mathbf{a} , A diffusion-limited case with exponentially increasing diffusivity upon delithiation. \mathbf{b} , A reaction-limited case with an exponentially increasing reaction rate upon delithiation. In both cases, the simulated XRD plots show fictitious phase separation during delithiation. Dashed lines on the XRD plot are when the peaks from the two fictitious phases are equally prominent. At this moment, the composition of each particle is averaged, equivalent to intra-particle relaxation (inter-particle lithium exchange is suppressed). These particle-averaged statistics show a bimodal particle distribution in the reaction-limited case, \mathbf{b} ut a unimodal distribution in the diffusion-limited case. \mathbf{c} , Schematic illustration of the conclusion on inhomogeneity evolution. \mathbf{d} , Generally, any interface limitation and strong composition dependency can produce inter-particle inhomogeneity. Simulation results show that interface limitation from an ohmic element can also produce autocatalytic behaviour similar to Butler-Volmer kinetics. These mechanisms can be distinguished from the electrochemical profile of rate versus overpotential η . $j_{0,\Omega}$ is defined by analogy to the Butler-Volmer equation (Supplementary Equation (61)).

intra-particle heterogeneity is more generally described as interface limitation and bulk limitation, respectively. Reaction kinetics in the form of Butler–Volmer kinetics is merely one specific case of interface limitation. An autocatalytic ohmic interfacial resistance, representing contributions from surface layers or electrical contacts, produces similar ensemble heterogeneity as demonstrated in Fig. 4d. In the present case of NMC, the current versus voltage plots (Supplementary Fig. 3c,d) indicate that the dominant component is a Butler–Volmer type. This observation, however, does not entirely exclude other possible interfacial contributions.

Data-driven model extraction also indicates an autocatalytic reaction rate. For quantitative confirmation of our phase-evolution picture based on autocatalytic reactions, we develop a workflow (summarized in Fig. 5) that integrates data from X-ray microscopy, operando XRD and electrochemistry. The first step of the workflow (Fig. 5a) is to select the relevant model class based on data, either reaction- or diffusion-limited models based on the statistics from X-ray microscopy. We use a Bayesian model selection³¹ method as detailed in Supplementary Section 7. The histogram comparison in Fig. 5a favours the reaction-limited model, consistent with our analysis in Fig. 4.

Next, we extract the best specific model (from the reaction-limited class) by fitting it to the operando XRD data (Fig. 5b). The time scale in operando XRD encodes information on kinetics, especially rate dependencies critical for phase evolution. Examples of extracting rate constants do exist32, but what we need is a function, that is, a reaction rate with respect to the lithium fraction. Here, we devise a method to extract this kinetic function by solving an inverse problem for the variable coefficient in a Fokker-Planck equation that describes the time evolution of the probability distribution of lithium fractions^{1,2,33,34} (Supplementary Sections 8.1 and 8.2). The temporal evolution of XRD-implied probability densities from three different C-rates are fitted simultaneously while imposing the electrochemical conditions (current in this case; see Supplementary Section 8 for voltage), as shown in Fig. 5b. The composition-dependent lithium reaction rate in the form of Butler-Volmer kinetics (Supplementary Equation (2)) is thereby extracted.

The exchange current j_0 versus lithium composition curve (Fig. 5c), found from the fitting process in Fig. 5b, indeed shows an exponentially sensitive composition dependence, especially near the full lithium fraction. The steep j_0 dependency on the lithium fraction primarily determines the fitting quality, indicating that this feature is insensitive to other details in the model such as particle size distribution or other stochastic noise such as thermal fluctuations (Supplementary Section 6). We note that the j_0 curve shape (inset of Fig. 5c) is insensitive to the particle morphology (platelets or agglomerates) and the measurement technique (using the potentiostatic intermittent titration technique (PITT) or electrochemical impedance spectroscopy (EIS)). This consistency provides further evidence that the rapidly varying interfacial exchange current is responsible for the autocatalytic and autoinhibitory behaviour.

Generality for intercalation reactions. The steep increase in exchange current with the lithium vacancy concentration, particularly near the fully lithiated state, is a general tendency for intercalation reactions. We confirm this by measuring j_0 in NMC111, NMC532, NMC 83:5:12 and LMR-NMC by EIS (Extended Data Fig. 4). In terms of charge-transfer theory¹⁵, a transition state mediates the lithium intercalation and deintercalation reactions. If we consider that this transition state must exclude s vacancy sites for the reaction, then the exchange current is modified by a $(1-c)^s$ factor where c and 1-c are the fractions of lithium and vacancies, respectively³⁵ (site counting due to localized electronic species could further increase the exponent). In situations where the solvation shell of Li⁺ becomes sizable, s would increase and augment the autocatalytic effect. This atomistic

yet generally applicable argument is consistent with the similar direction-dependent peak bifurcation behaviour seen in the multiple NMC compositions we verify with operando experiments (summarized in Table 1); it is also consistent with the literature observations in NCA ^{15,17,19,22} and other NMC compositions ^{18,20,21}. A similar argument could be applied for compositions near full delithiation, but such compositions are not accessible for most layered oxides. For a broader scope of materials and particle geometries, whether inter-particle inhomogeneity will develop due to electro-autocatalysis will depend on the autocatalytic rate (see Supplementary Equation (3) describing the competition between autocatalysis and thermodynamic equilibration) and whether or not the particle delithiation is interface limited.

Non-equilibrium model predicts a threshold rate. With the j_0 curve obtained in Fig. 5c, we use our reaction-limited population-dynamics model to make general predictions on the evolution of single-phase intercalation electrodes. A major feature of the predicted phase-evolution diagram (Fig. 5d) is that the fictitious two-phase region exists only in the delithiation direction and only above a certain threshold C-rate. This feature is consistent with the notion of fast and slow reaction regimes, which we defined earlier based on empirical observations. The vanishing width of the 'two-phase' region near the threshold implies that the apparent separation cannot be resolved at rates only slightly above the threshold C-rate. The general feature of an asymptotically increasing gap with C-rate is consistent with some literature observations¹⁶.

The threshold C-rate for fictitious phase separation is predicted to increase as the exchange current becomes larger (that is, if the curve in Fig. 5c moves upwards) and also as delithiation starts in a partially delithiated state. The ratio between the reaction rate (C-rate) and the equilibration rate (j_0) determines the 'fastness' of the current-driven reaction (Supplementary Equation (4)), making the threshold C-rate proportional to j_0 . For galvanostatic delithiation in NMC or NCA, the C-rate: j_0 ratio is highest near a lithium fraction of 1.0. If one avoids this stage by starting the reaction at a partially reacted state, the extent of fictitious phase separation is mitigated, accompanied by a higher threshold rate, as shown in the magnified plot in Fig. 5d.

Finally, our model explains the inconsistently reported phase separation in previous studies, mostly seen only in the first cycle. The slow rates (usually C/5 or less^{15,17,19}) typically used for operando XRD measurements make it generally less likely to be well above the threshold rate where peak bifurcation would be most visible. In systems where j_0 could be inherently low, for example, due to carbonate surface layers¹⁹, the threshold should be much lower and thus easier to access with a low C-rate. Regarding the first-cycle effect, one factor could be the common practice of not fully lithiating during the first cycle¹⁹. Figure 5d suggests that even a modest extent of incomplete lithiation at the beginning of charge can notably diminish fictitious phase separation. This explanation is also consistent with the recent report in NCA where second-cycle fictitious phase separation is seen after nearly complete re-lithiation²². As another factor for the first-cycle effect, it is often found in those studies that the overpotential decreases after the first cycle^{17,19}. This effect may be interpreted as an increase in j_0 after the first cycle, which then would require a higher C-rate than the first cycle for observing a similar separation effect in later cycles (due to an increase in the threshold rate). The decrease in the second-cycle overpotential in those studies starting from the very early stage of charging suggests an interfacial origin rather than a change in diffusivity¹⁷.

Implications for non-equilibrium chemical thermodynamics.

The rate and path dependencies of the fictitious, particle-by-particle, phase separation clearly indicate that the destabilization of the single-phase material is a kinetically induced instability. This directly contradicts the Duhem–Jougeut theorem³⁶⁻³⁸ which states that

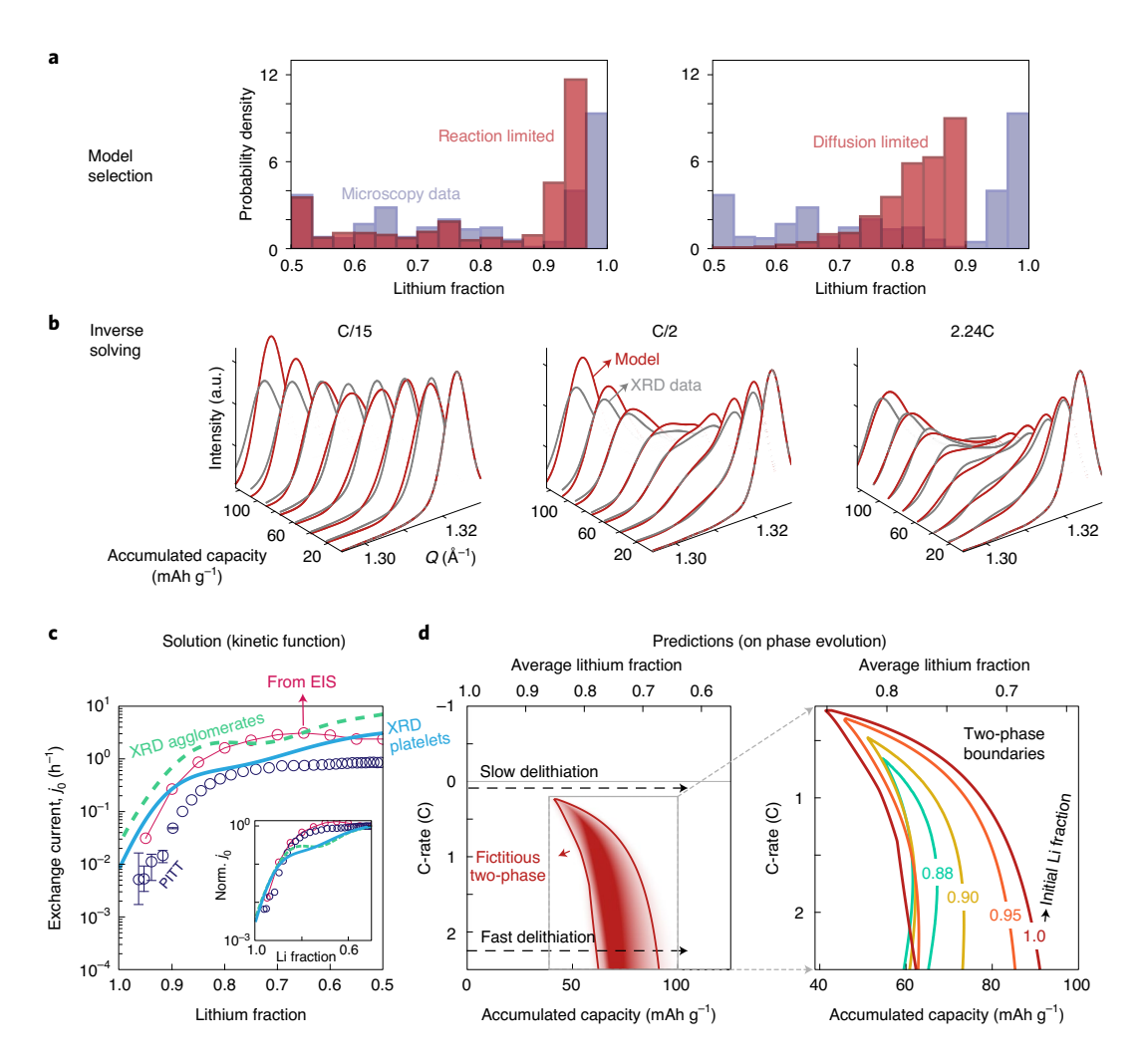


Fig. 5 | Multiple datastream workflow for quantitative model extraction and prediction. a, The model class selection step. The model histogram (red) is the optimal one found in each model class (Supplementary Section 7). The inter-particle distribution in the fast-delithiation X-ray microscopy data (violet histogram, from Fig. 2a) clearly rejects the diffusion-limited case. **b**, Simultaneous model fitting to the operando XRD data from varied C-rates to extract the kinetic function underlying the population-evolution dynamics. The fitting result is from platelet particle data; only a selected number of time points are shown. **c**, The exchange current function obtained from solving the inverse problem. Compared are results from agglomerate particles, from inverse solving (green dashed line) and also from using PITT (navy open circles; Supplementary Section 9) and EIS (magenta open circles; Supplementary Section 10). Regardless of the scale, all curves show a similar composition dependency as seen in the normalized plot (inset). **d**, Non-equilibrium model based on i_0 of platelets (sky blue solid line in **c**) predicting a phase-evolution diagram. Above a delithiation rate threshold, conditions exist at which fictitious separation occurs (shaded region) for reactions starting at a lithium fraction of 1.0. The shade density indicates the prominence of the probability peak associated with the second fictitious phase. The magnified plot on the right shows shrinkage in the fictitious-phase-separating region when delithiation starts at a partially delithiated state. The contour labels indicate the average lithium fraction at the start of delithiation.

thermodynamic stability is equivalent to kinetic stability for chemical reactions. This century-old classical theorem has implicitly justified the use of equilibrium stability criteria even for driven open systems (such as battery electrodes), as seen in population-dynamics models^{1,33,34,39} and linear kinetics-based reaction-diffusion models^{40,41}. It was recently shown that the Duhem–Jougeut theorem breaks down for any explicit non-linearities in reaction rates with respect to concentration or overpotential (solo-autocatalysis)^{2,42}, which we experimentally confirm in the present study. The same theoretical work also formulated a modified theory for stability¹², where kinetic stability requires a negative autocatalytic rate (Supplementary Equation (3)) in addition to thermodynamic stability. This theory is consistent with the autoinhibitory behaviour during lithiation observed regardless of the C-rate.

Autoinhibition was previously proposed to explain the suppression of phase separation in $LiFePO_4$ (ref. 3). The ambiguity in the $LiFePO_4$ system due to the time scale of phase separation (see

Supplementary Section 13 for a detailed account) is not present in NMC, since it is a single-phase material. Overall, our work establishes a unified theory of ensemble stabilization and destabilization driven by electro-autocatalytic reactions: phase-separating materials can be driven into a solid solution, and likewise single-phase materials can be driven into a fictitious phase separation.

Concluding remarks. We resolve the long-standing paradox of anomalous phase separation observed in single-phase layered oxides. The apparent separation is traced to inter-particle heterogeneity caused by electro-autocatalytic reactions in a particle ensemble. This finding suggests a general framework for the population dynamics of intercalation materials that exhibit strongly composition-dependent reaction rates. Depending on the rate (fast or slow) and path (autocatalytic or autoinhibitory directions), reaction pathways can drive the population to multiple dynamical fixed points that resemble phase separation, only to disappear when the current is reduced or

Table 1 | Generality of autocatalysis and highly composition-dependent charge-transfer resistance

Composition	Bifurcation during fast delithiation	Bifurcation during fast lithiation	Steep j _o vs Li
NMC111	0	Χ	0
NMC532	0	Χ	0
NMC 83:5:12	0	Χ	0
Li/Mn-rich NMC	0	Χ	0
NMC111 dual layer	0	0	-

O, observed; X, not observed. Operando XRD data can be found in Fig. 1 (NMC111), Extended Data Figs. 1 (NMC532), 2 (NMC 83:5:12) and 3 (Li/Mn-rich NMC), and Supplementary Fig. 26 (dual layer). Data from j_0 measurements are compiled in Extended Data Fig. 4.

reversed. Population dynamics is therefore a crucial component even for single-phase materials, not just for phase-separating materials. In battery applications, these considerations are crucial for understanding inter-particle inhomogeneity, even in thicker electrodes (see Supplementary Fig. 28 and Supplementary Video 2).

Our study challenges the prevailing paradigm in materials science that associates heterogeneity with diffusion-limited mechanisms. We demonstrate instead how diffusion-controlled systems tend to suppress composition variations between particles, and demonstrate the importance of considering the strong concentration dependence of interfacial (reaction) kinetics. We also challenge the conventional thinking that ensemble stability is determined by the equilibrium phase diagram even when reactions are occurring. Our results demonstrate that a rate-dependent stability criterion (Supplementary Equation (3)) is necessary.

Online content

Any methods, additional references, Nature Research reporting summaries, source data, extended data, supplementary information, acknowledgements, peer review information; details of author contributions and competing interests; and statements of data and code availability are available at https://doi.org/10.1038/s41563-021-00936-1.

Received: 24 May 2020; Accepted: 18 January 2021; Published online: 08 March 2021

References

- Dreyer, W. et al. The thermodynamic origin of hysteresis in insertion batteries. Nat. Mater. 9, 448–453 (2010).
- Zhao, H. & Bazant, M. Z. Population dynamics of driven autocatalytic reactive mixtures. *Phys. Rev. E* 100, 012144 (2019).
- Lim, J. et al. Origin and hysteresis of lithium compositional spatiodynamics within battery primary particles. Science 353, 566–571 (2016).
- Liu, H. et al. Capturing metastable structures during high-rate cycling of LiFePO₄ nanoparticle electrodes. Science 344, 1252817 (2014).
- Zhang, X. et al. Rate-induced solubility and suppression of the first-order phase transition in olivine LiFePO₄. Nano Lett. 14, 2279–2285 (2014).
- Li, Y. et al. Current-induced transition from particle-by-particle to concurrent intercalation in phase-separating battery electrodes. *Nat. Mater.* 13, 1149–1156 (2014).
- Zhang, W. et al. Kinetic pathways of ionic transport in fast-charging lithium titanate. Science 367, 1030–1034 (2020).
- Gonzalez-Rosillo, J. C. et al. Lithium-battery anode gains additional functionality for neuromorphic computing through metal-insulator phase separation. Adv. Mater. 32, 1907465 (2020).
- Yin, S.-C., Rho, Y.-H., Swainson, I. & Nazar, L. F. X-ray/neutron diffraction and electrochemical studies of lithium de/re-intercalation in Li_{1-x}Co_{1/3}Ni_{1/3}Mn _{1/3}O₂ (x=0→1). Chem. Mater. 18, 1901–1910 (2006).
- Choi, J. & Manthiram, A. Role of chemical and structural stabilities on the electrochemical properties of layered LiNi_{1/3}Mn_{1/3}Co_{1/3}O₂ cathodes. *J. Electrochem. Soc.* 152, A1714–A1718 (2005).
- Kondrakov, A. O. et al. Charge-transfer-induced lattice collapse in Ni-rich NCM cathode materials during delithiation. *J. Phys. Chem. C* 121, 24381–24388 (2017).

- Seidlmayer, S. et al. First-cycle defect evolution of Li_{1-x}Ni_{1/3}Mn_{1/3}Co_{1/3}O₂ lithium ion battery electrodes investigated by positron annihilation spectroscopy. *J. Power Sources* 336, 224–230 (2016).
- Weber, R., Fell, C. R., Dahn, J. R. & Hy, S. Operando X-ray diffraction study of polycrystalline and single-crystal Li, Ni_{0.5}Mn_{0.3}Co_{0.2}O₂. J. Electrochem. Soc. 164, A2992–A2999 (2017).
- Bang, H. J., Joachin, H., Yang, H., Amine, K. & Prakash, J. Contribution of the structural changes of LiNi_{0.80}Co_{0.15}Al_{0.05}O₂ cathodes on the exothermic reactions in Li-ion cells. *J. Electrochem. Soc.* 153, A731–A737 (2006).
- Yoon, W.-S., Chung, K. Y., McBreen, J. & Yang, X.-Q. A comparative study on structural changes of LiCo_{1/3}Ni_{1/3}Mn_{1/3}O₂ and LiNi_{0.8}Co_{0.15}Al_{0.05}O₂ during first charge using in situ XRD. *Electrochem. Commun.* 8, 1257–1262 (2006).
- Zhou, Y.-N. et al. High-rate charging induced intermediate phases and structural changes of layer-structured cathode for lithium-ion batteries. Adv. Energy Mater. 6, 1600597 (2016).
- Robert, R., Bünzli, C., Berg, E. J. & Novák, P. Activation mechanism of LiNi_{0.80}Co_{0.15}Al_{0.05}O₂: surface and bulk operando electrochemical, differential electrochemical mass spectrometry, and X-ray diffraction analyses. *Chem. Mater.* 27, 526–536 (2015).
- Li, J., Downie, L. E., Ma, L., Qiu, W. & Dahn, J. R. Study of the failure mechanisms of LiNi_{0.8}Mn_{0.1}Co_{0.1}O₂ cathode material for lithium ion batteries. *J. Electrochem. Soc.* 162, A1401–A1408 (2015).
- Grenier, A. et al. Reaction heterogeneity in LiNi_{0.80}Co_{0.15}Al_{0.05}O₂ induced by surface layer. Chem. Mater. 29, 7345–7352 (2017).
- Märker, K., Reeves, P. J., Xu, C., Griffith, K. J. & Grey, C. P. Evolution of structure and lithium dynamics in LiNi_{0.8}Mn_{0.1}Co_{0.1}O₂ (NMC811) cathodes during electrochemical cycling. *Chem. Mater.* 31, 2545–2554 (2019).
- Lee, W. et al. New insight into Ni-rich layered structure for next-generation Li rechargeable batteries. Adv. Energy Mater. 8, 1701788 (2017).
- Grenier, A. et al. Intrinsic kinetic limitations in substituted lithium-layered transition-metal oxide electrodes. J. Am. Chem. Soc. 142, 7001–7011 (2020).
- Li, W., Reimers, J. & Dahn, J. In situ X-ray diffraction and electrochemical studies of Li_{1-x}NiO₂. Solid State Ion. 67, 123–130 (1993).
- 24. Pillot, C. The rechargeable battery market and main trends 2016–2025. In 34th Annual International Battery Seminar & Exhibit (2017).
- Newman, J. & Tiedemann, W. Porous-electrode theory with battery applications. AIChE J. 21, 25–41 (1975).
- Ferguson, T. R. & Bazant, M. Z. Phase transformation dynamics in porous battery electrodes. *Electrochim. Acta* 146, 89–97 (2014).
- Smith, R. B. & Bazant, M. Z. Multiphase porous electrode theory. J. Electrochem. Soc. 164, E3291–E3310 (2017).
- Wang, Q. et al. Thermal runaway caused fire and explosion of lithium ion battery. J. Power Sources 208, 210–224 (2012).
- Tsai, P.-C. et al. Single-particle measurements of electrochemical kinetics in NMC and NCA cathodes for Li-ion batteries. *Energy Environ. Sci.* 11, 860–871 (2018).
- Fraggedakis, D. et al. A scaling law to determine phase morphologies during ion intercalation. *Energy Environ. Sci.* 13, 2142–2152 (2020).
- Wasserman, L. Bayesian model selection and model averaging. J. Math. Psychol. 44, 92–107 (2000).
- Arai, H. et al. Phase transition kinetics of LiNi_{0.5}Mn_{1.5}O₄ electrodes studied by in situ X-ray absorption near-edge structure and X-ray diffraction analysis. *J. Mater. Chem. A* 1, 10442–10449 (2013).
- Dreyer, W., Guhlke, C. & Huth, R. The behavior of a many-particle electrode in a lithium-ion battery. *Physica D* 240, 1008–1019 (2011).
- Dreyer, W., Guhlke, C. & Herrmann, M. Hysteresis and phase transition in many-particle storage systems. Continuum Mech. Therm. 23, 211–231 (2011).
- Bazant, M. Z. Theory of chemical kinetics and charge transfer based on nonequilibrium thermodynamics. Acc. Chem. Res. 46, 1144–1160 (2013).
- 36. Duhem, P. Traité Élémentaire de Mécanique Chimique Pondée sur la Thermodinamique (Librairie Scientifique A. Hermann, 1897–1899).
- Jouguet, E. Observations sur les principes et les théorémes généraux de la statique chimique. J. Éc. Polytech. 21, 61–180 (1921).
- 38. Kodepudi, D. & Prigogine, I. in *Modern Thermodynamics: From Heat Engines to Dissipative Structures* 2nd edn, 310–313 (John Wiley & Sons, 2014).
- Guhlke, C., Gajewski, P., Maurelli, M., Friz, P. K. & Dreyer, W. Stochastic many-particle model for LFP electrodes. *Continuum Mech. Therm.* 30, 593–628 (2018).
- Tang, M., Carter, W. C. & Chiang, Y.-M. Electrochemically driven phase transitions in insertion electrodes for lithium-ion batteries: examples in lithium metal phosphate olivines. *Annu. Rev. Mater. Res.* 40, 501–529 (2010).
- 41. Carati, D. & Lefever, R. Chemical freezing of phase separation in immiscible binary mixtures. *Phys. Rev. E* **56**, 3127–3136 (1997).
- Bazant, M. Z. Thermodynamic stability of driven open systems and control of phase separation by electro-autocatalysis. Faraday Discuss. 199, 423–463 (2017).

Publisher's note Springer Nature remains neutral with regard to jurisdictional claims in published maps and institutional affiliations.

 $^{\odot}$ The Author(s), under exclusive licence to Springer Nature Limited 2021

Methods

Sample preparation. NMC111 secondary particles were obtained from Samsung Advanced Institute of Technology (see ref. ⁴³ for characterization). Primary particles with a platelet morphology were synthesized by a molten-salt method as detailed in the Supplementary Information (Supplementary Section 1). Electrode slurries were prepared by mixing the active material, carbon black (Super P, Alfa Aesar) and binder (polyvinylidene fluoride, MTI) in a 4:4:2 weight ratio, together with *N*-methyl-2-pyrrolidone (Sigma-Aldrich). Electrode sheets were prepared by coating the slurry onto carbon-coated aluminium foils, using a doctor blade with a 100 µm nominal thickness, which were subsequently dried in a vacuum oven at 70 °C overnight and then calendered. The final thickness of the electrodes was typically around 20 µm.

Pouch cells were assembled in an argon-filled glove box using polymer-cladded aluminium pouches; a 25- μ m-thick separator (H2512-0460M-D, Celgard), 1 cm² electrode sheet, a 170- μ m-thick lithium foil, LP-40 electrolyte (100 μ l; Gotion), a nickel (negative) tab and an aluminium (positive) tab were vacuum-sealed in the pouch.

The NMC111 cells used in this study were pre-cycled at C/20 up to a state-of-charge of 50% (formation cycle). The cutoff during charging was done based on the target capacity; during discharging the lower voltage cutoff was set to either 2 or 2.5 V, after which the voltage was held constant. The state-of-charge in this study was defined based on the theoretical capacity assuming full lithium occupation, corresponding to a gravimetric capacity of 278 mAh g⁻¹.

Samples for X-ray microscopy were prepared by cycling primary platelet particles in pouch cells to facilitate the lithium-exchange quenching process. During this process, the NMC111 electrodes were removed from the cell within 2 min after electrochemically reaching the target state-of-charge and current interruption. The removed NMC111 electrode sheets were rinsed several times with diethyl carbonate to remove any residual electrolyte or salt. NMC111 particles were removed from the electrode sheet by sonication and were drop-cast onto carbon membrane-coated copper grids. An argon atmosphere was maintained for the entire process, including the sample transfer to the instrument which was done with an air-free holder (Gatan).

Operando X-ray diffraction. XRD measurements were conducted at the 11-3 beamline at the Stanford Synchrotron Radiation Lightsource. A pouch cell holder, where the electrode stack region of the pouch cell is pressurized between two thin beryllium plates, was used to maintain pressure during the electrochemical cycling while having access for X-ray measurements (design shown in Supplementary Fig. 25). The Coulomb-counted states-of-charge in the pouch cells were consistent with those determined from XRD (Supplementary Fig. 16), indicating proper pressurization of the cell. A beam energy of 12.7 keV was used for the experiments (with a Raxyonics 225 detector) and the aluminium peak was used to calibrate the momentum transfer parameter $Q = \frac{4\pi \sin \theta}{\lambda}$ in the diffraction data for each individual sample (where θ is the scattering angle and λ is the X-ray wavelength). The pouch cells were cycled with an SP300 galvanostat/potentiostat (BioLogic). The electrochemical and XRD data were synchronized using timestamps; the electrochemical charge capacity corresponding to each XRD pattern was determined by interpolating between the two nearest timestamps. Subtraction of the diffusive background in the XRD patterns was done by fitting a polynomial function to the baseline, leaving only the Bragg peak information in the plots.

Scanning transmission X-ray microscopy (STXM). STXM measurements were conducted at the 7.0.1 COSMIC beamline at the Advanced Light Source. Images were raster scanned with a 50 nm step size and 2 ms dwell time at energies at the Ni $\rm L_{3.2}$ absorption edge. A zone plate with an outer zone width of 45 nm was used for all scans. Beam energy shifts relative to the reference spectra were calibrated by imaging pristine NMC111 particles. Transmission images of each energy were aligned by detecting the edges of the particles with a Sobel filter and subsequently converted to optical density images. The absorption spectrum of each pixel was linearly decomposed using two reference spectra (Supplementary Fig. 8) and by imposing non-negative constraints for the coefficients. Using these coefficients, the lithium composition and relative thickness of each pixel were determined. The final particle images were rendered using an HSV colouring scheme: the hue was set to show the composition ranging from red (1.0 lithium fraction) to green (0.5 lithium fraction); the value (brightness) was set to describe the relative particle thickness; and the saturation was set to maximum.

Simulation and modelling. Procedures for the simulation, model extraction and inverse problem solving are detailed in the Supplementary Information.

Data availability

Data represented in Fig. 1 can be accessed at: https://doi.org/10.7910/DVN/EMJFMU. Data represented in Fig. 2 can be accessed at: https://doi.org/10.7910/DVN/AVP215. Additional data for this study are available from the authors upon reasonable request.

Code availability

Code for solving the Fokker–Planck equation can be found at: https://github.com/hbozhao/e-autocat. Additional code is available from the authors upon reasonable request.

References

 Gent, W. E. et al. Persistent state-of-charge heterogeneity in relaxed, partially charged Li_{1-x}Ni_{1/3}Co_{1/3}Mn_{1/3}O₂ secondary particles. Adv. Mater. 28, 6631–6638 (2016).

Acknowledgements

This work was supported by the Toyota Research Institute through the Accelerated Materials Design and Discovery programme. The characterization aspect of the work was supported by the Assistant Secretary for Energy Efficiency, Vehicle Technologies Office of the US Department of Energy under the Advanced Battery Materials Research Program. J.H. was funded through the Korea Institute of Science and Technology (2E30993; 2V08350). We would like to acknowledge support from the following people: S. Kalirai from the Lawrence Berkeley National Laboratory for assistance in STXM experiments; C. J. Takacs from SLAC for assistance in the operando XRD holder design and instrument operation; C.-N. Yeh from Stanford University for help in atomic force microscopy; X. Xu from Stanford University for taking SEM images; S. Ahn, J.-H. Park and S.-K. Doo from Samsung Advanced Institute of Technology for providing the NMC111 and Li-Rich NMC materials; J. Haag and H. Sommer from BASF for providing the NMC 83:5:12 material; Microvast for providing single-crystalline NMC test materials; Y. Zhang and M. Scott for providing the air-free transfer holder for STXM; P. Csernica and E. Carlson for finding errors in the manuscript. The authors used resources of the following facilities: the Stanford Synchrotron Radiation Lightsource, SLAC National Accelerator Laboratory, supported by the US DOE, Office of Science, Office of Basic Energy Sciences (DE-AC02-76SF00515); the Advanced Light Source, a US DOE Office of Science User Facility (DE-AC02-05CH11231); the Stanford Nano Shared Facilities, supported by the National Science Foundation (ECCS-2026822); and the 1D XRS KIST-PAL beamline at the Pohang Accelerator Laboratory.

Author contributions

J.H. obtained the first preliminary data and initiated the project with his ideas. J.P. synthesized the materials, prepared the samples and led the experiments. J.P., K.L. and S.D.K. performed the XRD measurements. K.L. designed the operando XRD holder. J.P., S.D.K. and C.-C.C. carried out the STXM measurements with assistance from Y.-S.Y. Analysis of the XRD and STXM data was conducted by S.D.K. The model was constructed by H.Z. and S.D.K. The simulation was conducted by H.Z. who also performed the inverse problem solving. H.Z., S.D.K. and C.-C.C. interpreted the modelling results. S.D.K. drafted the manuscript. All authors reviewed and commented on the manuscript. M.F.T. supervised the XRD experiments. Y.-S.Y. and D.A.S. supervised the STXM experiments. M.Z.B. and R.D.B. supervised the simulation and modelling. W.C.C. supervised the overall project.

Competing interests

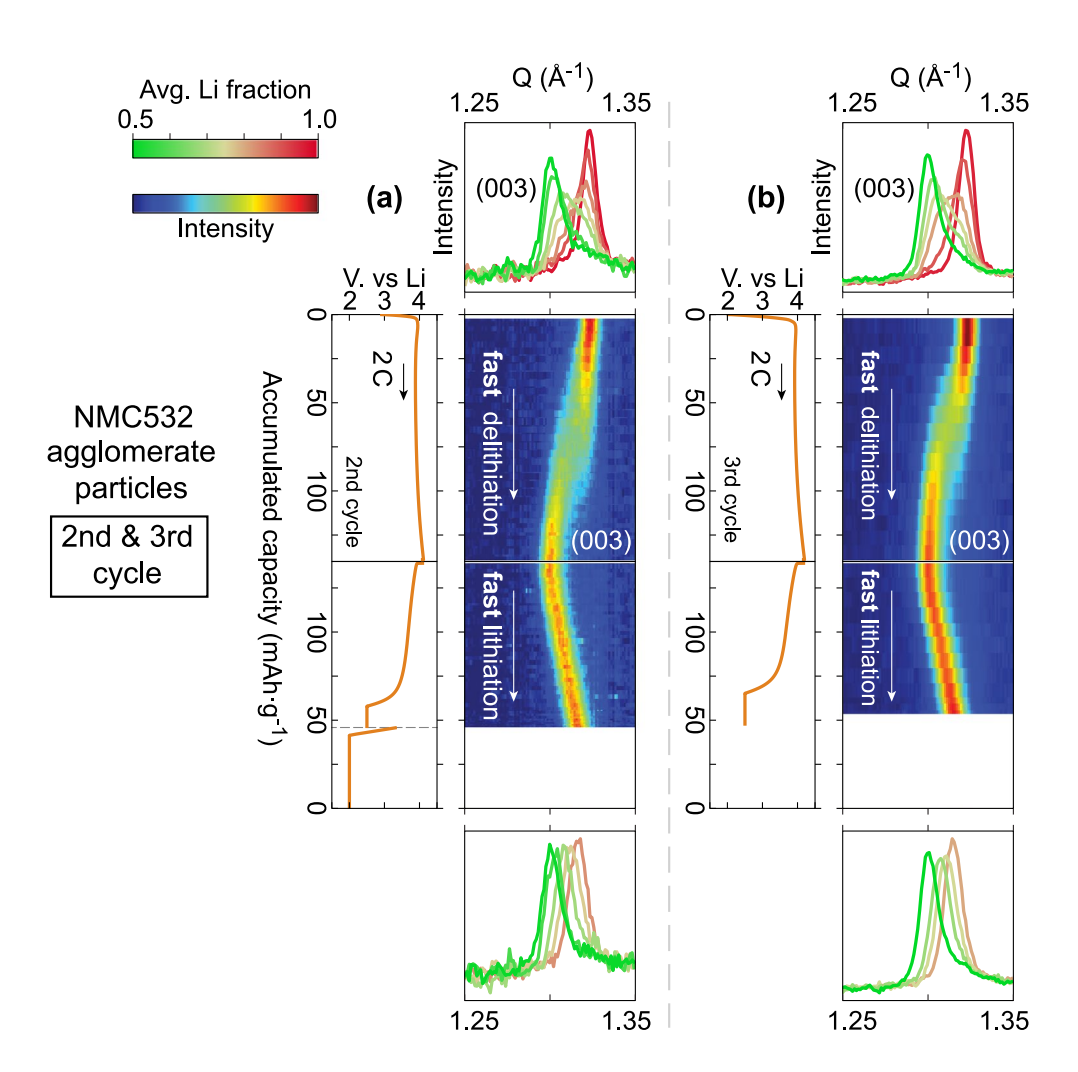
The authors declare no competing interests.

Additional information

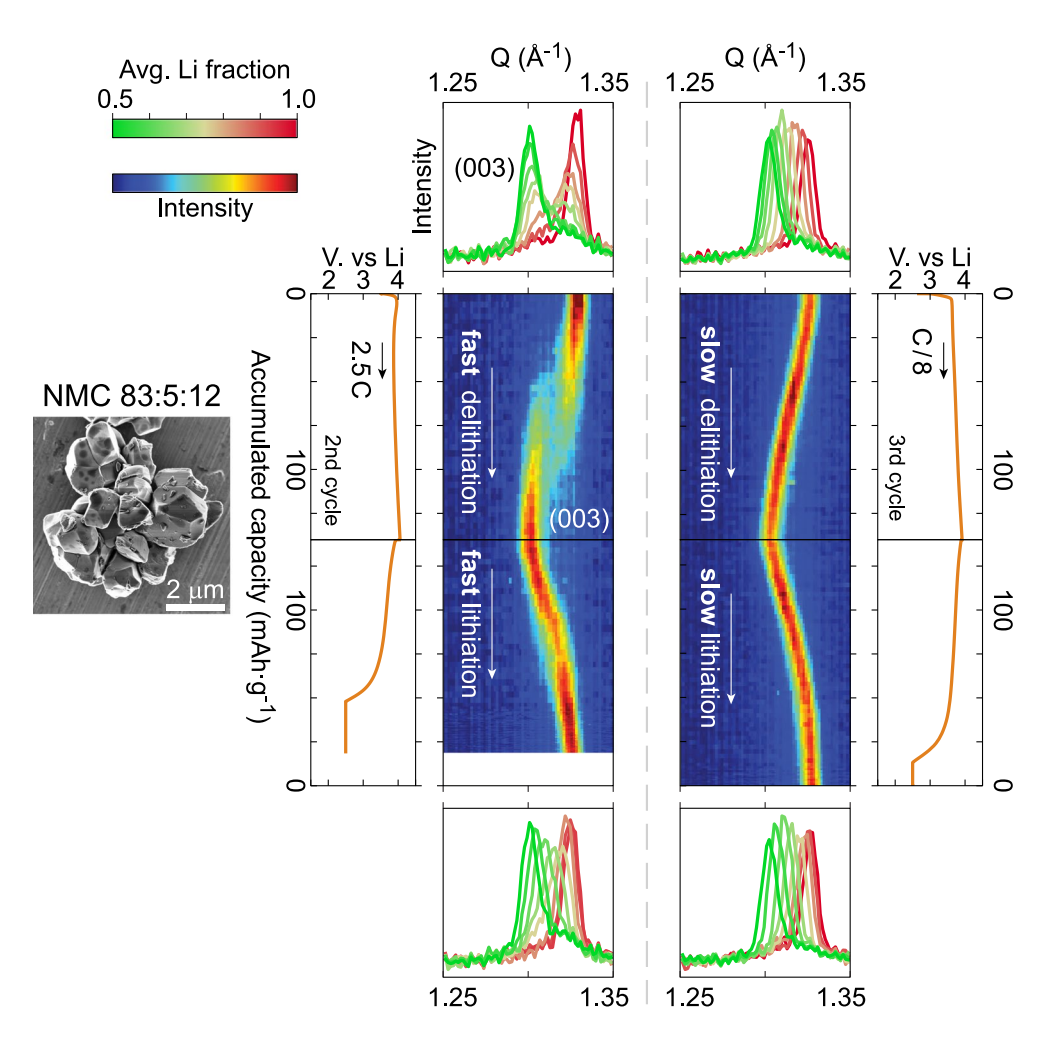
Extended data is available for this paper at https://doi.org/10.1038/s41563-021-00936-1.

Supplementary information The online version contains supplementary material available at https://doi.org/10.1038/s41563-021-00936-1.

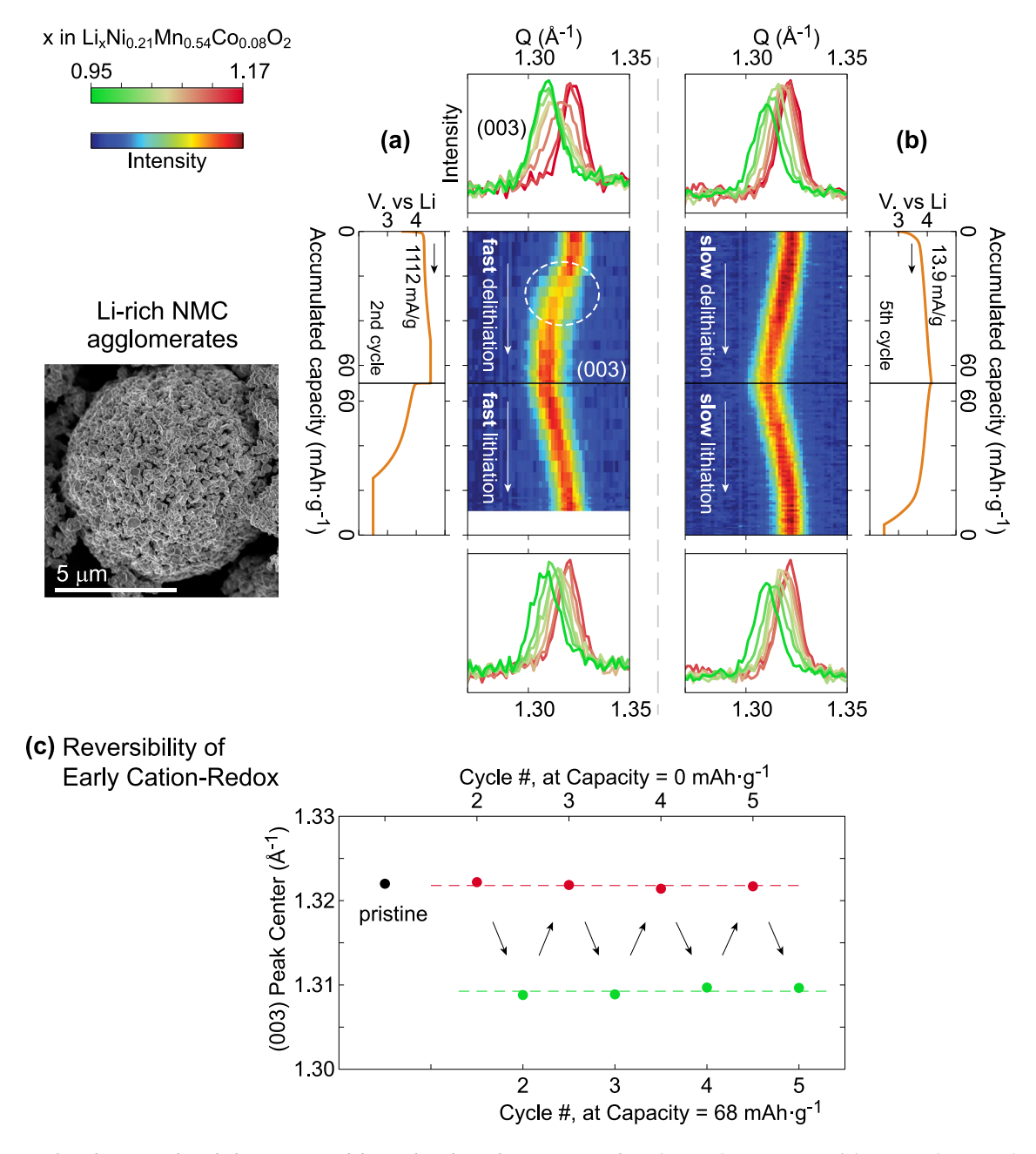
Correspondence and requests for materials should be addressed to J.H., M.Z.B. or W.C.C.



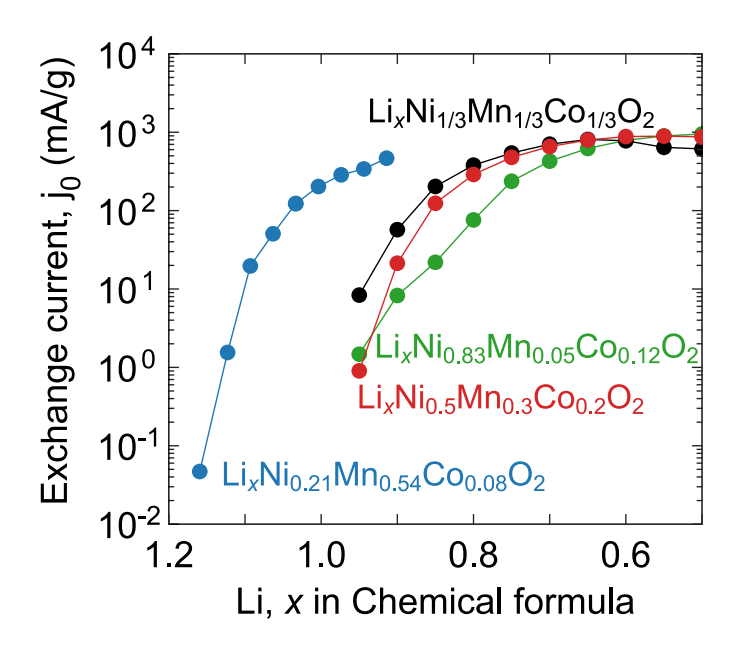
Extended Data Fig. 1 | Autocatalysis behavior in $Li_x(Ni_{0.5}Mn_{0.3}Co_{0.2})O_2$ agglomerate particles. Fast cycling (2C) during the **a** second and **b** 3rd cycle. Prior to the second cycle, NMC532 was lithiated to a charge-counted Li fraction of 0.985 with a voltage hold at 2.5 V. After the 2nd cycle measurement, the cell was fully lithiated with a voltage hold at 2.0 V (during which diffraction measurements were not available at the beamline). Using the identical sample, the 3rd cycle was measured.



Extended Data Fig. 2 | Autocatalysis behavior in $Li_x(Ni_{0.83}Mn_{0.05}Co_{0.12})O_2$ single crystalline particles. Prior to the 2nd cycle, NMC 83:5:12 was lithiated to a charge-counted Li fraction of 1 with a voltage hold at 2.5 V.



Extended Data Fig. 3 | Autocatalysis behavior in Li-rich layered oxide agglomerate particles. The initial composition of the material was $Li_{1,17}(Ni_{0,21}M)$ $n_{0.54}Co_{0.08})O_2$. Prior to the 2nd cycle, the material was charged up to a specific capacity of 108.3 mAh/g and discharged by the same amount (voltage hold at 2.5 V at the end of discharge). This capacity, which is within the cation-redox region, was selected to conduct the experiment while avoiding the irreversible and complex structural changes associated with anion-redox. The contrast between the fast delithiation case (1112 mA/g; upper panels in **a**) and all other conditions (lower panels in **a** and all panels in **b**) indicate autocatalysis behavior similar to other NMC compositions. The autocatalytic effect manifests at a much earlier stage of delithiation, compared with other NMC compositions. **c** The (003) peak positions monitored during the operando XRD experiment, confirming the reversibility in the early capacity region of cation-redox.



Extended Data Fig. 4 | Compilation of mass-specific exchange current curves obtained from EIS. All curves were obtained using particles in electrodes made with the same recipe as used for the operando XRD experiments. Agglomerate particles were used for NMC111, NMC532, and Li/Mn-rich NMC. Single crystalline particles were used for NMC 83:5:12.